



Iron binding to human heavy-chain ferritin

This is the peer reviewed version of the following article:

Original:

Pozzi, C., DI PISA, F., Bernacchioni, C., Ciambellotti, S., Turano, P., Mangani, S. (2015). Iron binding to human heavy-chain ferritin. ACTA CRYSTALLOGRAPHICA. SECTION D, BIOLOGICAL CRYSTALLOGRAPHY, 71(Pt 9), 1909-1920 [10.1107/S1399004715013073].

Availability:

This version is available http://hdl.handle.net/11365/1006830 since 2017-05-15T17:34:44Z

Published:

DOI:10.1107/S1399004715013073

Terms of use:

Open Access

The terms and conditions for the reuse of this version of the manuscript are specified in the publishing policy. Works made available under a Creative Commons license can be used according to the terms and conditions of said license.

For all terms of use and more information see the publisher's website.

(Article begins on next page)

Iron binding to human heavy chain ferritin

Authors

Cecilia Pozzia, Flavio Di Pisaa, Caterina Bernacchionibc, Silvia Ciambellottibc, Paola Turanobc and Stefano

Mangani^{ac}*

^aDipartimento di Biotecnologie, Chimica e Farmacia, University of Siena, Via Aldo Moro 2, Siena, 53100,

^bDipartimento di Chimica, University of Florence, Via Della Lastruccia 3, Sesto Fiorentino, Firenze, 50019,

Italy

^cCERM, University of Florence, Via Della Lastruccia 3, Sesto Fiorentino, Firenze, 50019, Italy

Correspondence email: stefano.mangani@unisi.it

universal mechanism for iron oxidation in all ferritins.

Synopsis The time-lapse crystal structures of human H chain ferritin loaded with iron show the distribution of the substrate metal ion within the catalytic site. The comparison of these data with our previous x-ray structures of Rana catesbeiana M ferritin points to a number of shared and unshared features

of the active sites of the two proteins that contribute to the ongoing debate on the possible existence of a

Maxi ferritins are ubiquitous iron-storage proteins with a common cage architecture made of 24 Abstract

identical subunits of five α-helices that drive the iron biomineralization through a catalytic Fe(II) oxidation

occurring at oxidoreductase sites (OS). Structures of the iron-bound human H ferritin were solved at high

resolution by freezing ferritin crystals at different time intervals after exposure to a ferrous salt. Multiple

binding sites were identified that define the iron path from the entry ions channels to the oxidoreductase site.

Similar data are available on another vertebrate ferritin, the M protein from Rana catesbeiana. The

comparative analysis of the iron sites in the two proteins identifies new reaction intermediates and underlines

clear differences in the pattern of ligands that define the additional iron sites that precede the oxidoreductase

binding sites along this path. Stopped-flow kinetics assays revealed that human H ferritin, in contrast to its

Rana catesbeiana counterpart, has different levels of activity. The role of the different pattern of transient

iron binding sites in the OS is discussed with respect to the observed differences in activity across the

species.

1. Introduction

1

Ferritins are ubiquitous chemical reactors that control the biosynthesis and dissolution of caged hydrated ferric mineral (E.C. 1.16.3.1). They also function as antioxidants by retrieving iron ions released from degraded iron proteins preventing the occurrence of Fenton-like chemistry (Theil *et al.*, 2013).

The 24 subunit ferritins, called maxi-ferritins, self-assemble to form a nanocage having an outer diameter of approximately 120 Å, while the diameter of the internal cavity is around 80 Å (Liu & Theil, 2005). The ferritin nanocage is characterized by having 432 (O, octahedral) point symmetry with three 4-fold, four 3-fold and six 2-fold axes (Crichton & Declercq, 2010). Thousands of iron atoms can be stored into the inner cavity as iron mineral obtained by catalytic oxidation of Fe(II) by dioxygen or hydrogen peroxide in the protein oxidoreductase sites (OS) (Figure 1), where the substrates are coupled to obtain Fe(III) mineral precursors (Theil *et al.*, 2013; Theil, 2011). In vertebrates, ferritin usually functions as a hetero-polymer composed of two distinct subunits, the H (Heavy, about 21 kDa) chain and the L (Light, about 19 kDa) chain that co-assemble in H:L ratios that are tissue specific (Arosio *et al.*, 2009). Ferritin rich in L-chain that lacks oxidoreductase activity is found in tissues involved in long-term storage of iron such as the liver or spleen, while H-chain-rich ferritin, having oxidoreductase activity, is found in the tissues with more active iron metabolism such as the muscle.

Iron binding sites in maxi-ferritins have been identified by conventional x-ray crystallography only for the extremophile Archaea *Pyrococcus furiosus* (Tatur *et al.*, 2007), for the prokaryote *Escherichia Coli* (Stillman *et al.*, 2001) and for the eukaryotic pennate diatom *Pseudo-nitzschia* (Marchetti *et al.*, 2009). In other ferritins the identification of iron binding sites has been more difficult due to the quite fast turnover occurring also in the crystal that prevented the use of soaking-freezing experiments. Only recently a different approach has successfully revealed iron binding to *Rana catesbeiana* M ferritin (RcMf) (Bertini *et al.*, 2012; Pozzi *et al.*, 2015). These studies have identified the existence of several iron binding sites defining a possible pathway for Fe(II) ions from the entry channels to the OS and have highlighted the role of several residues along this path.

There is an intense ongoing debate in the literature about the mechanism(s) by which the different ferritins are operating. Recently, a so-called unifying mechanism for all ferritins has been proposed (Ebrahimi *et al.*, 2012a; Honarmand *et al.*, 2015), but other views are also supported by experimental evidence (Bou-Abdallah *et al.*, 2014; Bradley *et al.*, 2014; Pozzi *et al.*, 2015).

The wide ferritin panorama still misses the identification of the iron binding sites in a mammalian ferritin. To fill this gap, we report here the results of our crystallographic determination of the iron adducts to human H ferritin (HuHf) obtained by applying the same experimental method used in our previous RcMf study (Pozzi *et al.*, 2015). Time-lapse anomalous data have allowed us to follow the progressive population of a series of iron binding sites in a recombinant form of HuHf.

HuHf and RcMf share about 64% identity; the residues identified as active site ligands in RcMf (i.e., Glu103, Glu58, His61 and Glu23) are all conserved in HuHf (the HuHf sequence numbering is shifted +4 with

respect to RcMf as shown in Figure S1), but there are meaningful differences in the amino acid composition in the OS residues proposed as additional transient iron binding sites in RcMf. The comparative analysis of the x-ray crystal structures and kinetic data for HuHf and RcMf presented here, shows changes in the number and position of these additional iron sites and in reaction rates. The implications for the proposed ferritin mechanism(s) are discussed.

2. Materials & methods

2.1. Protein expression and purification

RcMf was expressed as previously described (Pozzi *et al.*, 2015). The gene coding sequence for HuHf was custom synthesized (Genscript, USA) and subcloned into the pET-9a expression vector using the NdeI and BamHI restriction sites.

Transformants were selected on LB agar added by 50 mg/L kanamycin. Bacterial culture was grown at 37° C on LB medium supplemented of 50 mg/L kanamycin. Protein over-expression was induced with 0.2 mM IPTG (isopropyl-β-D-1-thiogalactopyranoside) when the cell density reached an A₆₀₀ of 0.6 and incubated at 30° C. The cells were harvested by centrifugation after 16 h of induction and resuspended in buffer A (20 mM TRIS pH 7.7, 1 mM EDTA (ethylenediamine tetraacetic acid), 0.15 M NaCl, 0.1 mM PMSF (phenyl methane sulfonyl fluoride hydrochloride)). The intracellular content was liberated by sonication and the resulting suspension was centrifuged at 18500 x g for 45 minutes at 6° C to remove the insoluble fraction. The supernatant of the resulting crude extract was incubated at 60°C for 10 min and the heat stable fraction was further purified by ammonium sulfate precipitation (50-60% saturated fractions), anion exchange chromatography and size exclusion chromatography as previously described for RcMf (Pozzi *et al.*, 2015).

2.2. Crystallization

Purified HuHf in 20 mM Tris pH 7.7 and 0.15 M NaCl was concentrated to 13.4 mg/mL. Crystals of native HuHf were grown using the hanging drop vapor diffusion technique at 297 K. Drops were prepared by mixing equal volumes (2 μL) of HuHf and a precipitant solution composed of 2.0 M MgCl₂ and 0.1 M bicine at pH 9.0 for a final pH value of about 8.0. Octahedrally shaped crystals of 50 – 100 μm size grew in 3-6 days. Crystallization of HuHf has been also obtained under strict anaerobic conditions by using the same procedure already reported for RcMf (Pozzi *et al.*, 2015). These crystals have been used as a control for the oxidation state and coordination environment of iron in the aerobic crystals.

A time controlled iron loading study was performed by allowing solid-to-solid Fe(II) ion diffusion from $[(NH_4)_2Fe(SO_4)_2]\cdot 6H_2O$ (Mohr's salt) grains to HuHf crystals of approximately the same size ($\sim 100 \,\mu\text{M}$) for the monitored exposure time of 1, 5, 15 and 30 minutes, and up to 8 minutes for the anaerobic crystals, followed by flash freezing in liquid nitrogen, as already reported for RcMf (Pozzi *et al.*, 2015).

2.3 Data collection, structure solution and refinement.

Complete data sets were collected at the Diamond Light Source (DLS) beamline I04-1 on a Pilatus-2M detector at 100 K. Data were integrated using the program Mosflm 7.0.4 (Leslie, 2006) and scaled with Scala (Evans, 2006; Evans, 2011) from the CCP4 suite (Winn *et al.*, 2011). HuHf crystals belonged to the cubic space group F432 with cell parameters of a \approx 185 Å, varying slightly among the different crystals. Data collection and processing statistics are reported in Table 1. Anomalous difference maps have been computed from the single wavelength data, exploiting the iron anomalous signal, still present at 0.920 Å (13.477 keV; $f^*\sim$ -0.298 e-, f^* , \sim 1.351 e⁻) that nevertheless provides very clear anomalous maps due to the high quality and redundancy of the data collected. All the iron binding sites found from these maps, have been later fully confirmed by lower resolution datasets collected in two wavelengths measurement mode (Fe-K edge and remote) at Elettra (Trieste – Italy), on crystals treated with iron under exactly the same conditions.

Phasing was performed by molecular replacement, using the software Molrep (Vagin & Teplyakov, 1997) from the CCP4 suite. A subunit of human H ferritin (PDB code 3AJO) was used as searching model excluding non-protein atoms and water molecules. The positions of the iron ions were determined from the anomalous difference Fourier maps computed using the program FFT from the CCP4 suite. The anomalous signals corresponding to iron ions were between 6 and 40 σ in the anomalous difference maps.

The structures were refined with the program Refmac 5.8 (Murshudov *et al.*). The refinement protocol involved a sequence of iterative manual rebuilding of the model and maximum likelihood refinement. Manual rebuilding and modeling of the missing atoms into the electron density was performed with the molecular graphic software Coot (Emsley *et al.*, 2010). Partial occupancies for the iron or magnesium ions, for other ligands and for several amino acid residues were adjusted in order to obtain atomic displacement parameters close to those of neighboring protein atoms in fully occupied sites. The occupancies of the water molecules or other ligands bound to metal ions were kept the same as the parent metal ion. The program ARP/wARP was used for water molecules addition (Langer *et al.*, 2008). The final models have been inspected manually and checked with the programs Coot and Procheck (Laskowski *et al.*, 1993). Final refinement statistics are reported in Table 2. All the figures were generated using CCP4mg (McNicholas *et al.*, 2011).

2.4. Stopped-flow kinetics.

Addition of 1-4 Fe(II) ions per subunit (Bernacchioni *et al.*, 2014; Bernacchioni *et al.*, 2015; Theil *et al.*, 2014) in HuHf and RcMf, was monitored as the change in A_{650 nm} (diferric peroxo; DFP) or A_{350 nm} (diferric oxo/hydroxo species, DFO(H)) after rapid mixing (less than 10 ms) of equal volumes of 100 μM protein subunits (4.16 μM protein cages) in 200 mM 3-(N-morpholino) propane sulfonic acid (MOPS), 200 mM NaCl, pH 7.0, with freshly prepared solutions of 100, 200, 300 and 400 μM ferrous sulfate in 1 mM HCl in a UV/visible stopped-flow spectrophotometer (SX.18MV stopped-flow reaction analyzer, Applied

Photophysics, Leatherhead, UK). Routinely, 4,000 data points were collected during the first 5 s. Initial rates of DFP and DFO(H) species formation were determined from the linear fitting of the initial phases (0.01–0.03 s) of the change in absorbance at 650- and 350-nm, respectively. The decay rate of the DFP species was fitted with a monoexponential function of the fall in intensity at 650 nm (Tosha *et al.*, 2012).

2.5. Transmission Electron Microscopy (TEM)

Recombinant ferritin protein cages (3 μM) were mineralized with ferrous sulfate (80 Fe(II)/subunit) in 100 mM MOPS, 100 mM NaCl, pH 7.0. Two different procedures were followed: i) a total of 80 Fe(II)/subunit was added in a single step; ii) three sequential additions were performed (20 Fe(II)/subunit, 20 Fe(II)/subunit, 40 Fe(II)/subunit). After each addition, the solutions were incubated for 2 h at room temperature and then overnight at 4 °C to complete the iron mineralization reaction. For TEM tests, solutions of mineralized HuHf and RcMf cages were dropped and dried on a Cu grid covered by holey carbon film. Bright-field TEM images were collected on a Philips CM12 microscope operating at 80 kV (Bernacchioni *et al.*, 2014).

2.6. PDB codes

Final coordinates and structure factors of HuHf loaded with iron ions for 1, 5, 15 and 30 minutes have been deposited in the Protein Data Bank under the accession codes 4P03, 4ZJK, 4OYN and 4YKH, respectively.

3. Results

3.1 Overall structure of human H ferritin

A series of HuHf structures were obtained at high resolution by following an established protocol that allows us to use time-lapse crystallography to appreciate the succession of the iron binding events (Pozzi *et al.*, 2015). Crystals of iron-free HuHf, were mixed with crystalline ferrous ammonium sulfate powder (Mohr's salt) and frozen after 1, 5, 15, 30 minutes of free diffusion of the Fe(II) ions in the crystallization drop, in the presence of the second reaction substrate, dioxygen (see Materials & methods section).

The structure of iron-free HuHf (not described) was obtained as reference structure and shows the same quaternary structure of all other maxi ferritins that consists of the assembly of 24 identical subunits to form a hollow cage. The asymmetric unit contains a single HuHf subunit which represents the spatial and time average of all subunits of the molecules in the crystal. The HuHf subunit reported in Figure 1, shows the characteristic four-helix bundle (helices 1 to 4) tertiary structure completed by the fifth helix (helix 5) (Theil *et al.*, 2013).

Each of the four structures determined for this work contains a variable number of metal ions (Mg (II) and/or Fe(II)/Fe(III)); the chemical nature of the metal was discriminated according to the anomalous signal detected. The oxidation state of iron ions was more elusive and was derived from the comparison with the structure obtained under anaerobic conditions (*vide infra*). The refined structures are all nearly complete as,

according to the electron density for all structures, the polypeptide chain has been built starting from residue 5 to residue 176. No significant changes in the fold of the HuHf subunit were observed upon exposure to the iron salt.

3.2 HuHf iron binding at the ferroxidase at different diffusion times.

The structure obtained after free diffusion of Fe(II) ions for about **1 minute** under aerobic conditions has been refined to 1.34 Å resolution. Figure 2A reports a view of the OS with the iron ions found from the anomalous difference map computed from data collected above the Fe K-edge. Superimposed to the anomalous map are the 2Fo-Fc and the Fourier difference maps. The largest anomalous signal (28 σ) identifies an iron ion bound at the iron site 1 (Fe1) defined by Glu27 (monodentate ligand from helix 1), Glu62 (monodentate ligand, from helix 2) and His65 (from helix 2). A water molecule (Wat1 in Figure 2A) bound to Fe1 is clearly visible. A much weaker anomalous signal (6.5 σ) corresponds to the Fe ion bound to the nearby site 2 (Fe2) where it is held by Glu62 carboxylate forming the bridge to Fe1 and by coordination bonds to Glu107 (as bidentate ligand from helix 3). Fe1 and Fe2 refine to occupancies of about 0.7 and 0.2, respectively and are located at a distance of 3.48 Å. These two sites are the same as the Fe1 and Fe2 sites found in RcMf. At variance with the RcMf structure obtained in the same experimental conditions (Pozzi *et al.* 2015) no Mg(II) ions from the crystallization solution are found bound into the OS. In addition, a large maximum between Fe1 and Fe2 that cannot be accounted for by a bridging water/hydroxide molecule is present in the Fourier difference map (Figure 2A). This maximum indicates that the completion of the coordination spheres of Fe1 and Fe2 might involve other ligands.

Figure 2B shows a view of the ferroxidase site after completing the refinement that reports our best interpretation of the difference Fourier map. The elongated maximum of continuous electron density between Fe1 and Fe2 (Figure 2A) suggests the presence of a biatomic molecule and persists even when two water molecules at partial occupancy (too close to be independent) were inserted. We were then tempted to model such density as a peroxide anion or a dioxygen molecule. Finally, our best model consists of a biatomic "dioxygen" molecule bound to Fe1 and Fe2 in a μ - η_2 : η_2 configuration (bridging side-on) with the same occupancy of Fe2 (0.2), and of a bridging water/hydroxide at the same occupancy of Fe1 (0.7) (hidden by "dioxygen" in Figure 2B). A second bridging water/hydroxide at low occupancy (0.3) can account for residual electron density between the iron ions (Wb2 in Figure 2B). As it can be seen from Figure 2B, this model accounts for the maxima of the Fo-Fc map in that part of the cavity.

Inspection of the anomalous difference map (see Figure 2A) reveals the presence of a third Fe ion (Fe3, 5.5 σ) bound to the nearby Gln58 residue found disordered over two positions (Fe-bound and unbound). Fe3 is close to Fe2 (2.73 Å) and can be refined to 0.3 occupancy. Here the Fo-Fc map shows several maxima difficult to interpret revealing disorder in this site (Figure 2A). In addition to the Gln58 side chain, one conformer of Glu107 is within coordination distance from Fe3 and the well ordered side chain of Glu62 lies

at about 2.65 Å. Two water molecules and one "dioxygen" molecule with the same occupancy as the metal ion can be refined as Fe3 ligands to reach six-coordination. However, after refinement, the residual Fo-Fc map still presents very diffuse maxima of positive electron in the surroundings of Fe3. A fourth iron ion (Fe4) is found bound at 0.3 occupancy to the nearby His57 residue that sprouts into the cage cavity at about half way between the 3-fold pore (22 Å) and the 4-fold pore (24 Å) (not shown in Figures 2A,B).

The **1 minute** exposure experiment has been repeated twice in order to verify the reproducibility of the quite puzzling results obtained and indeed, the Fourier maps obtained display the same features.

However, although suggestive, our interpretation of the electron density maps cannot be claimed as clear evidence of the trapping of the dioxygen substrate into the HuHf OS before reaction (see discussion). On the other hand, the interpretation described above leads to the best minimum of the refinement quality indicators and it can be framed as the superposition of different states occurring in HuHf subunits: in about 30 % of them no iron is bound; in about 70 % of them the OS Fe site 1 is occupied by iron and in about 20 % also the OS Fe site 2 (empty in 80 % of the cases) binds iron. In the 50 % of the cases where only site 1 is occupied a water molecule completes the Fe1 coordination, while in the 20 % of the cases where both sites 1 and 2 are occupied, a dioxygen molecule might bind in μ - η_2 : η_2 coordination mode to both Fe1 and Fe2. It should be noted that the shape of the electron density interpreted as dioxygen is the same or even better when compared to the electron density of "dioxygen" molecules bound to enzymes like naphthalene dioxygenase (PDB: 107M) (Karlsson *et al.*, 2003) or cytochrome P450cam (PDB:1DZ8,2A1M) (Nagano & Poulos, 2005; Schlichting *et al.*, 2000).

The Fe site 3 might represent the 30 % of the subunits where the Fe1 and Fe2 sites are not yet occupied by iron. This is supported by the double conformation of Glu107 that appears to take Fe3 from Gln58 and drive it to the Fe2 site (Figures 2A,B).

In any case, this crystal structure confirms that Gln58 is involved in iron shuttling into the OS Fe1 and Fe2 iron binding sites, in a dynamic process evidenced by the structural disorder present in this portion of the cavity, as already suggested by our previous experiments on RcMf where His54 takes the role of Gln58 and on the RcMf H54/Q54 variant (Pozzi *et al.*, 2015). In other words, the different HuHf subunits of our crystal are trapped in different states related to their interaction with Fe(II) ions providing a superposition of images that show the conformational variability of the residues involved in iron processing.

The anomalous difference map of HuHf measured after **5 minutes** of Fe(II) free diffusion, reveals a clearer picture of the ferroxidase site, although some disorder is still present. The map confirms the sites already observed in the previous structure, but now the occupancies are much higher (Figure 3A). Fe1 is fully occupied while Fe2, Fe3 and Fe4 reach 50 % occupancy. Also the coordination spheres of all iron ions are better defined as shown in Figure 3B. Fe1 displays a 5+1 coordination sphere with five ligands (Glu27, Glu62, His65, Wb1 and Wat1) arranged in a square pyramidal geometry (His65 at the apex) and a further water molecule (Wb2) at longer distance that forms an asymmetric second bridge to Fe2. Fe2 coordination

can be described as trigonal bipyramid with Glu62, Glu107 (considering the bidentate Glu107 as one ligand) and Wb1 in the basal plane and Wb2 and Wat2 at the apices. The same Fe1 and Fe2 ligands have been already observed to bind iron ions in RcMf in the same fashion (Pozzi *et al.*, 2015) with the exception of Wb2 that has never been observed in other ferritins. In the 5 minutes structure, the "biatomic" molecule bridging Fe1 and Fe2 in the 1 minute structure has been replaced by the Wb1 species (water/hydroxide). Both Wb1 and Wb2 have gained full occupancy, Wb1 is H-bonded to the side chain of Gln141, while Wb2 is at contact distance to Val110. The Fe1-Fe2 distance is 3.49 Å. A hydrogen bonding network links Gln141, the bidentate Fe2 ligand Glu107 and Tyr34. Tyr34 and Gln141 together with the other residues involved in Fe1 and Fe2 binding are highly conserved in H/M-type ferritins (Ebrahimi *et al.*, 2012b) (see Figure S1).

The position of Fe3 has now changed to reach a different and better-defined coordination environment (see Figures 3A,B). Fe3 is in a new position located 6.61 Å away from Fe2 being bound at coordination distances from Gln58 (now ordered) and Glu61, the only protein ligands in this site, and surrounded by four water molecules that complete a quite regular octahedral coordination. The involvement of Glu61 in HuHf in the attraction of iron towards the OS is similar to what observed for the corresponding Glu57 in RcMf.

Fe4 is at 5.08 Å from Fe3 and it is bound to Glu61 that bridges it to Fe3. His57 and four water molecules are the remaining ligands to define nice octahedral coordination geometry also for this site.

Increasing the Fe(II) diffusion time (15 and 30 minutes) brings no further changes into the iron binding sites in the OS and surroundings. All iron ions, Fe1 to Fe4, maintain the same coordination environments, indicating that after about five minutes a dynamical equilibrium has been reached in the protein crystals.

In summary, the occupancy of Fe1 to Fe4 does not vary after 5 minutes of exposure to the Mohr's salt. The Fe1 results about 70% occupied after 1 minute and fully occupied from 5 minutes onwards. On the contrary, the Fe2 occupancy ranges from about 20%, in the structures determined after short diffusion time, to a maximum of about 50%. The same occurs for Fe3 and Fe4 occupancies that achieve a 50% maximum. At variance with the observations made about iron-bound RcMf (Pozzi *et al.*, 2015), both Wb1 and Wb2 molecules make asymmetric bridges between Fe1 and Fe2, both being closer to Fe2. There are not evident structural reasons to justify this behavior. A possible explanation could be that in all HuHf structures (except the 1 minute one), we are observing a mixed valence Fe1(II)-Fe2(III) cluster, instead of the Fe1(II)-Fe2(II) cluster suggested by the RcMf crystal structures (Pozzi *et al.*, 2015). The increased positive charge of the site can also explain the presence of Wb2 (possibly a hydroxide anion), never observed in RcMf.

The high resolution structure (1.2 Å) of iron-bound HuHf, after 8 minutes of exposure to Mohr's salt, from crystals obtained under strict anaerobic conditions (data not shown) has been used as a check for the oxidation state of iron in the aerobically grown crystals. This structure shows iron ions bound only to Fe sites 1 and 2 with occupancy of about 80% or Fe1 and of about 30% for site 2. The Fe1-Fe2 distance is 3.52 Å and, more importantly, only one water/hydroxide molecule is found symmetrically bridging the two irons, at

variance with the aerobic crystals. Fe1 and Fe2 adopt the same coordination geometry observed for RcMf (Pozzi *et al.*, 2015).

3.3 3-fold symmetry channels

The three fold symmetry channels have been identified as main entrance of iron ions in the protein shell (Haldar *et al.*, 2011; Theil, 2011). The structure of iron-free HuHf shows two Mg(II) hexa-aquaions, arising from the crystallization buffer, inside this negatively charged protein pore defined by the side chains of the three symmetry-related Asp131, Glu134 and Thr135 residues. A third Mg(II) hexa-aquaion is found just beyond the channel on the internal protein surface. The positions of these magnesium ions in the three fold pore results remarkably consistent to those previously reported on HuHf (Masuda *et al.*, 2010). The same three magnesium hexa-aquaions have been constantly observed also in the structure of HuHf exposed to Fe(II) ions for one and five minutes. On the contrary, in the structures determined after fifteen and thirty minutes of iron loading, two Fe(II)-hexa-aquaions have replaced the Mg(II) aquaions inside the channel as indicated by the strong anomalous peaks present in these sites (Figures 4A,B). The occupancy for both Fe(II) aquaions inside the channel refines to 0.6. The observation of iron in the three fold channel has been previously reported after a longer exposure time to iron (sixty minutes) for the RcMf and its variant H54Q (Pozzi, *et al.*, 2015).

3.4. 4-fold symmetry channels

The 4-fold pores of the ferritin cage are defined by four helices 5 (Figure 1), from symmetry related subunits, that make a four-helix bundle around the 4-fold axes. The part of the 4-fold channel facing the external surface of the ferritin cage, is highly hydrophobic, as in RcMf, being constituted by four symmetry related Leu165 and Leu169. Like RcMf, the internal portion of the channel, has a hydrophilic character being constituted by four symmetry related His173 residues. In the iron-free HuHf structure two chloride ions (identified by the anomalous signal), coming from the crystallization buffer, are located above and below the plane of the four His173 residues.

The binding of iron ions into the four-fold channel develops with time. The anomalous difference map of the 1 minute HuHf structure shows a very weak trace of the presence of Fe ions bound to a tiny fraction (less than 10 %) of the His173 residues. However, after five minutes, the 4-fold pore results fully occupied by a Fe(II) ion bound to the four symmetry-related His173 defining the plane of a tetragonal bipyramid having at the apices one chloride anion and one water molecule directed towards the external and the internal surface of the cage, respectively (Figure 5). This kind of coordination environment for Fe bound to the 4-fold pore is

identical to that previously observed in iron-loaded RcMf (Pozzi *et al.*, 2015), consistent with the presence of Fe(II) ions in this pore. No iron transport into the inner cage occurs through these types of channels (Theil *et al.*, 2014).

3.5. Reactivity in solution.

In both RcMf and HuHf stopped flow-kinetic measurements reveal that the same intermediate species form during the reaction, although with different kinetics. With a stoichiometry of 1 Fe(II)/subunit the activity at the OS is essentially negligible for both proteins (Figure 6A,B). With 2 Fe(II)/subunit or more, we can clearly observe the formation of the DFP intermediate and its rapid decay through a monoexponential process as well as the formation of the ferric oxo species. The initial rate of formation in RcMf grows essentially linearly when passing from 2 to 4 Fe(II)/subunit (Figure 6B); the increase in initial rate is less regular for HuHf. While for the latter protein the formation rate of DFP is slightly faster at low Fe(II) ratio, it levels off with 4 Fe(II)/subunit. On the contrary, the exponential decay of DFP is always slower in the HuHf protein, and this difference increases by increasing the Fe(II)/subunit ratio (Figures 6A,B). The initial rate of formation of DFO(H) species grows linearly with the Fe(II)/subunit ratio but with different slopes for the two proteins (Figure 6B). In spite of the different rates of the catalytic reactions, the end product of the biomineralization reaction is an iron-oxo core of comparable size for the same iron/protein ratio: 4.74±0.26 nm for HuHf vs 5.37±0.29 nm for RcMf as shown in Figure 7.

4. Discussion

Observing iron binding sites in most vertebrate maxi-ferritins is made difficult by the quite fast reaction rates measured in solution (< 25 msec for RcMf) (Hwang *et al.*, 2000) that prevent the use of conventional soaking or co-crystallization approaches. We have then developed a solid-to-solid free diffusion technique that allows trapping iron ions in their diffusion pathways trough ferritin by freezing the protein crystals at different times after exposure to iron (Pozzi *et al.*, 2015).

The sequence of iron binding events monitored by our experiments reported here starts with the partial occupancy of the oxidoreductase sites 1 and 2 by iron; the higher occupancy for Fe1 observed in the 1 minute structure that reaches full occupancy after 5 minutes, confirms all previous thermodynamic (Bou-Abdallah *et al.*, 2002a; Bou-Abdallah *et al.*, 2003; Ebrahimi *et al.*, 2012a), and structural data (Pozzi *et al.*, 2015) about the higher affinity of this site for metal ions in vertebrate ferritins. This is easily explained by the three protein ligands present in Fe site 1 with respect to the two protein ligands present in Fe site 2 (Pozzi *et al.*, 2015; Treffry *et al.*, 1997). Selective population of a single site in the OS is also consistent with the kinetic data (Figures 6A,B) that, at variance with previous Mössbauer data (Bou-Abdallah et al., 2002b) show absence of any ferroxidase activity when 1 Fe(II)/subunit is added. Similarly, the observation of a high

affinity iron binding site, corresponding to the HuHf site 1 has been previously reported also in the structures of ferritin from other organisms, such as *Pseudo-nitzschia multiseries* (Marchetti *et al.*, 2009; Pfaffen *et al.*, 2013), *E. Coli* (Stillman *et al.*, 2001) and *Pyrococcus furiosus* (Tatur *et al.*, 2007).

The 1 minute crystal structure evokes a fascinating hypothesis about a possible binding mode for the substrate dioxygen into the OS and suggests that this substrate binds the dinuclear oxidoreductase center only when iron site 2 is occupied by Fe(II) ions, possibly linked to the movement of iron from the provisional site 3 to site 2. The μ - η_2 : η_2 side-on coordination mode to a first transition row metal ion has been observed for dioxygen or peroxide only in a Cu laccase (PDB: 3ZDW) and in model complexes of dinuclear copper centers (Mirica *et al.*, 2004; Mirica *et al.*, 2006). This binding mode of dioxygen might evolve in the peroxodiferric intermediate structure suggested by vibrational and XAS spectroscopies (structure E or G in Figure 3 of Hwang *et al.*, 2000).

The observation of a short Fe3-Fe2 distance in the 1 minute structure (2.73 Å) that lengthens to 6.61 Å in the 5 minutes structure, suggests that the former structure has trapped the Fe(II) ion (Fe3 in Figures 2A,B) approaching the empty Fe2 site, possibly dragging with it an already bound dioxygen molecule.

The similarity of the 5, 15 and 30 minutes HuHf structures tells that after a short time lapse, a dynamical equilibrium is reached in the iron diffusion inside the crystals and that a steady-state like situation is established. The incoming Fe(II) ions are processed and stored as ferric mineral inside the ferritin cage as indicated by the rusty color gained by the crystals with time.

Taken together, the time-lapse pictures from the present study delineate a pathway for the incoming Fe(II) ions that starts with the electrostatic attraction and hydrogen bonding interactions of the Fe(II) hexa-aqua ions to the Asp131 and Glu134 residues in the 3-fold pore and continues with Glu140, Glu61, His57 and Gln58 to reach the Fe1 and Fe2 sites.

The coordination of Fe1 and Fe2 sites observed in HuHf shows relevant differences with respect to the same sites in RcMf determined under the same experimental conditions. While Fe1 and Fe2 in RcMf are linked by a double symmetric bridge (Glu58 and a water/hydroxide molecule), a triple asymmetric bridge is found between Fe1 and Fe2 in HuHf (Glu62 and two water/hydroxide molecules; see Figure 3B). Furthermore, Fe1 in HuHf shows a 5+1 type of coordination sphere in contrast with RcMf where Wb2 (Figures 3A,B) is absent.

A possible explanation of such differences can be found by analyzing the only experimental findings that can be correlated to the oxidation state of the iron ions in our structures, namely the coordination distances and the iron coordination geometry.

The Fe1-Fe2 distance in all HuHf structures remains remarkably constant to the value of 3.49 Å that is the same (within error) as that found in mixed valence model compounds (3.53-3.62 Å)¹ (Majumdar *et al.*, 2013) and in the mixed valence structure of methane monoxygenase where a Fe(II)-Fe(III) distance of 3.4 Å has been reported (2.07 Å resolution) (Whittington & Lippard, 2001). The Fe1-Fe2 distance observed in HuHf is the same of that observed in the crystal obtained under anaerobic conditions, but differs from the same distances found in RcMf structures of similar resolution that appear longer and vary between 3.5 and 3.8 Å, suggesting the presence of a Fe(II)-Fe(II) dinuclear cluster in that case. Despite the similarity of the Fe1-Fe2 distance in aerobic and anaerobic HuHf, their coordination number and geometry differ, but in the anaerobic crystal their geometry is the same as that found in RcMf. In summary our data provide some support to the hypothesis that Fe1 and Fe2 form a mixed valence dinuclear cluster in aerobic HuHf after 5 minutes of exposure to iron under aerobic conditions. In other words the 1 minute structure is most probably showing the binding of Fe(II) ions, while the 5, 15 and 30 minutes structures may show the occurrence of a mixed valence Fe1-Fe2 cluster. Clearly, the distinction from a mixed valence from a fully reduced iron cluster cannot rest on crystallography alone, but the comparison between the HuHf and RcMf structures, obtained under the same experimental conditions, clearly show differences in coordination geometry and inter-metal distances indicating a different chemical environment for the iron ions in the two proteins.

The measured differences in the dependence of the reaction rates on iron concentration between RcMf and HuHf most probably reflect the different amino-acid composition of the OS and to the different chemical environment of the iron ions. Consequently, the slower rate of DFP decomposition in HuHf with respect to RcMf, provides support to our hypothesis of having possibly trapped intermediate dioxygen species in our structures.

As it can be appreciated from Figure 8, the replacement of RcMf residues Glu53, His54 and Asp140 with His57, Gln58 and Ala144, results in HuHf oxidoreductase site in the net loss of two negative charges and in different ligand strength towards iron ions. Consequently it is not surprising that the kinetic data show different profiles for the same iron loading of the two enzymes and markedly different decay rate of the DFP intermediate.

The differences between HuHf and RcMf do not end at the Fe1 and Fe2 sites. Figure 8 reports the superposition of the 15 minutes structures of HuHf and RcMf, showing the different number and coordination of iron ions to OS, that varies following the aminoacid variations of the two ferritins. For example, Fe3 in RcMf is bound only to His54, while in HuHf is bound to Gln58 and Glu61 and occupies a different locus. In RcMf, Fe4 is bound to Glu57 (the analogous residue of HuHf Glu61) and to Asp140. In HuHf Asp140 is substituted by the noon-coordinating Ala144, hence the fourth iron ion is bound to HuHf His57 that replaces Glu53 of RcMf. In the present structures, Glu61 is found bridging Fe3 and Fe4

_

¹ See Cambridge Structural Database codes NIXLIR and NIXLUD for mixed valence compounds where Fe(II)-Fe(III) distances are 3.53-3.62 Å; to be compared with ferric-oxo(hydroxo) bridged compounds were Fe(III)-Fe(III) distances are 3.1 Å; codes: NIXMAK, VARYOC10.

supporting the hypothesis that it plays a role in driving iron ions to/from the ferroxidase site (Ebrahimi *et al.*, 2012a; Lawson *et al.*, 1991).

In summary, both the crystallographic and stopped-flow data clearly show the existence of relevant structural and kinetic differences between RcMf and HuHf and confirm that beyond the Fe1 and Fe2 sites, that remain structurally constant, the additional iron binding sites follow the chemical characteristics of the amino acids present in the OS and play a relevant role in the enzymatic reaction. Based on the reported evidence, the postulated third iron binding site, common characteristic of all ferritins (Ebrahimi *et al.*, 2012a; Honarmand *et al.*, 2015), does not exist as a specific, well defined metal coordination site, but it is rather a region extending up to about 10 Å from the Fe1 and Fe2 sites where heterogeneous iron anchoring points in ferritins of different origin are present.

Acknowledgements We acknowledge the financial support of MIUR PRIN 2012 (contract number 2012SK7ASN). C.B. is the recipient of a post-doctoral fellowship funded by Ente Cassa di Risparmio di Firenze (contract number 2013.0494). The research leading to these results has received funding from the European Community's Seventh Framework Programme (FP7/2007-2013) under BioStruct-X (grant agreement No. 283570). We thank Diamond Light Source for access to beamline I04-1 (proposal number: BIOSTRUCTX_1358) and Elettra (Trieste, Italy) for provision of synchrotron radiation facilities. We also would like to thank all the staff of the synchrotron sources for assistance in using the beamlines.

References

Arosio, P., Ingrassia, R., & Cavadini, P. (2009). Biochim. Biophys. Acta 1790, 589-599.

Bernacchioni, C., Ciambellotti, S., Theil, E. C., & Turano, P. (2015). *Biochim. Biophys. Acta* (Epub ahead of print. DOI: 10.1016/j.bbapap.2015.02.011).

Bernacchioni, C., Ghini, V., Pozzi, C., Di, P. F., Theil, E. C., & Turano, P. (2014). ACS Chem. Biol. 9, 2517-2525.

Bertini, I., Lalli, D., Mangani, S., Pozzi, C., Rosa, C., Theil, E. C., & Turano, P. (2012). J. Am. Chem. Soc. 134, 6169-6176.

Bou-Abdallah, F., Arosio, P., Santambrogio, P., Yang, X., Janus-Chandler, C., & Chasteen, N. D. (2002a). *Biochemistry* **41**, 11184-11191.

Bou-Abdallah, F., Papaefthymiou, G.C., Scheswohl D.M., Stanga S.D., Arosio P., Chasteen N.D. (2002b) *Biochem J.* **364**, 57-63.

Bou-Abdallah, F., Arosio, P., Levi, S., Janus-Chandler, C., & Chasteen, N. D. (2003). J Biol Inorg. Chem. 8, 489-497.

Bou-Abdallah, F., Yang, H., Awomolo, A., Cooper, B., Woodhall, M. R., Andrews, S. C., & Chasteen, N. D. (2014). *Biochemistry* **53**, 483-495.

Bradley, J. M., Moore, G. R., & Le Brun, N. E. (2014). J.Biol. Inorg. Chem. 19, 775-785.

Crichton, R. R. & Declercq, J. P. (2010). Biochimica et Biophysica Acta - General Subjects 1800, 706-718.

Ebrahimi, K. H., Bill, E., Hagedoorn, P. L., & Hagen, W. R. (2012a). Nat. Chem. Biol. 8, 941-948.

Ebrahimi, K. H., Hagedoorn, P. L., van der, W. L., Verhaert, P. D., & Hagen, W. R. (2012b). *J. Biol. Inorg. Chem.* 17, 975-985.

Emsley, P., Lohkamp, B., Scott, W. G., & Cowtan, K. (2010). Acta Cryst. D66, 486-501.

Evans, P. (2006). Acta Cryst. D62, 72-82.

Evans, P. R. (2011). Acta Cryst. D67, 282-292.

Haldar, S., Bevers, L. E., Tosha, T., & Theil, E. C. (2011). J. Biol. Chem. 286, 25620-25627.

Honarmand, E. K., Hagedoorn, P. L., & Hagen, W. R. (2015). Chem. Rev. 115, 295-326.

Hwang, J., Krebs, C., Huynh, B. H., Edmondson, D. E., Theil, E. C., & Penner-Hahn, J. E. (2000). *Science* **287**, 122-125.

Karlsson, A., Parales, J. V., Parales, R. E., Gibson, D. T., Eklund, H., & Ramaswamy, S. (2003). *Science* **299**, 1039-1042.

Langer, G., Cohen, S. X., Lamzin, V. S., & Perrakis, A. (2008). Nat. Protoc. 3, 1171-1179.

Laskowski, R. A., MacArthur, M. W., Moss, D. S., & Thornton, J. M. (1993). J. Appl. Crystallogr. 26, 283-291.

Lawson, D. M., Artymiuk, P. J., Yewdall, S. J., Smith, J. M., Livingstone, J. C., Treffry, A., Luzzago, A., Levi, S., Arosio, P., Cesareni, G., & . (1991). *Nature* **349**, 541-544.

Leslie, A. G. (2006). Acta Cryst. **D**62, 48-57.

Liu, X. & Theil, E. C. (2005). Acc. Chem. Res. 38, 167-175.

Majumdar, A., Apfel, U. P., Jiang, Y., Moënne-Loccoz, P., & Lippard, S. J. (2013). Inorg. Chem. 53, 167-181.

Marchetti, A., Parker, M. S., Moccia, L. P., Lin, E. O., Arrieta, A. L., Ribalet, F., Murphy, M. E., Maldonado, M. T., & Armbrust, E. V. (2009). *Nature* **457**, 467-470.

Masuda, T., Goto, F., Yoshihara, T., & Mikami, B. (2010). Biochem. Biophys. Res. Commun. 400, 94-99.

McNicholas, S., Potterton, E., Wilson, K. S., & Noble, M. E. M. (2011). Acta Cryst. D67, 386-394.

Mirica, L. M., Ottenwaelder, X., & Stack, T. D. (2004). Chem. Rev. 104, 1013-1045.

Mirica, L. M., Rudd, D. J., Vance, M. A., Solomon, E. I., Hodgson, K. O., Hedman, B., & Stack, T. D. (2006). *J. Am. Chem. Soc.* **128**, 2654-2665.

Murshudov, G. N., Skubak, P. F., Lebedev. A.A., Pannu, N., Steiner, R., Nicholls, R., Winn, M., Long, F., & Vagin, A. (2011). *Acta Cryst.* **D67**, 355-367.

Nagano, S. & Poulos, T. L. (2005). J. Biol. Chem. 280, 31659-31663.

Pfaffen, S., Abdulqadir, R., Le Brun, N. E., & Murphy, M. E. (2013). J. Biol. Chem. 288, 14917-14925.

Pozzi, C., Di, P. F., Lalli, D., Rosa, C., Theil, E., Turano, P., & Mangani, S. (2015). Acta Cryst. D71, 941-953.

Rice, P., Longden, I., & Bleasby, A. (2000). Trends Genet. 16, 276-277.

Schlichting, I., Berendzen, J., Chu, K., Stock, A. M., Maves, S. A., Benson, D. E., Sweet, R. M., Ringe, D., Petsko, G. A., & Sligar, S. G. (2000). *Science* **287**, 1615-1622.

Stillman, T.J., Hempstead, P.D., Artymiuk, P.J., Andrews, S.C., Hudson, A.J., Treffry, A., Guest, J.R., & Harrison, P.M. (2001), *J.Mol. Biol.*, **307**, 587-603.

Tatur, J., Hagen, W. R., & Matias, P. M. (2007). J. Biol. Inorg. Chem. 12, 615-630.

Theil, E. C., Behera, R. K., & Tosha, T. (2013). Coord. Chem Rev. 257, 579-586.

Theil, E. C., Turano, P., Ghini, V., Allegrozzi, M., & Bernacchioni, C. (2014). J. Biol. Inorg. Chem. 19, 615-622.

Theil, E. C. (2011). Curr. Op. Chem. Biol. 15, 304-311.

Tosha, T., Behera, R. K., & Theil, E. C. (2012). Inorg. Chem. 51, 11406-11411.

Treffry, A., Zhao, Z., Quail, M. A., Guest, J. R., & Harrison, P. M. (1997). Biochemistry 36, 432-441.

Vagin, A. & Teplyakov, A. (1997). J. Appl. Crystallogr. 30, 1022-1025.

Whittington, D. A. & Lippard, S. J. (2001). J. Am. Chem. Soc. 123, 827-838.

Winn, M. D., Ballard, C. C., Cowtan, K. D., Dodson, E. J., Emsley, P., Evans, P. R., Keegan, R. M., Krissinel, E. B., Leslie, A. G., McCoy, A., McNicholas, S. J., Murshudov, G. N., Pannu, N. S., Potterton, E. A., Powell, H. R., Read, R. J., Vagin, A., & Wilson, K. S. (2011). *Acta Cryst.* **D67**, 235-242.

 Table 1
 Data collection and processing

Values for the outer shell are given in parentheses.

huHf + Fe(II)	1 min	5 min	15 min	30 min
PDB code	4Y08	4ZJK	4OYN	4YKH
Diffraction source	Diamond I04-1	Diamond I04-1	Diamond I04-1	Diamond I04-1
Wavelength (Å)	0.92	0.92	0.92	0.92
Temperature (K)	100	100	100	100
Detector	Pilatus 2M	Pilatus 2M	Pilatus 2M	Pilatus 2M
Crystal-detector distance (mm)	165	170	180	160
Rotation range per image (°)	0.20	0.20	0.20	0.20
Total rotation range (°)	100	100	100	100
Exposure time per image (s)	0.3	0.5	0.5	0.5

Space group, Z	F432, 4	F432, 4	F432, 4	F432, 4
No. of subunit in asymmetric unit	1	1	1	1
a,b,c (Å)	184.14	183.80	183.91	184.05
Mosaicity (°)	0.24	1.07	0.29	0.41
Resolution range (Å)	29.11-1.34 (1.41- 1.34)	31.07-1.56 (1.64- 1.56)	32.51–1.43 (1.51–1.43)	29.10-1.52 (1.60- 1.52)
Total No. of reflections	1205847 (172066)	437700 (36197)	990962 (142832)	809546 (102979)
No. of unique reflections	60022 (8623)	38257 (5431)	49578 (7123)	41531 (5956)
Completeness (%)	99.7 (100.0)	99.8 (99.1)	100.0 (100.0)	100.0 (100.0)
Anomalous Completeness (%)	99.8 (100.0)	99.0 (95.7)	100.0 (100.0)	100.0 (100.0)
Redundancy	20.1 (20.0)	11.4 (6.7)	20.0 (20.1)	19.5 (17.3)
Anomalous Redundancy	10.6 (10.3)	5.9 (3.4)	10.5 (10.3)	10.3 (8.8)
$\langle I/\sigma(I)\rangle$	28.2 (8.0)	25.0 (3.6)	27.9 (7.1)	25.8 (7.0)
$R_{ m rmeas} \dot{\underline{ au}}$	0.072 (0.414)	0.062 (0.510)	0.072 (0.438)	0.082 (0.434)
Overall <i>B</i> factor from Wilson plot (\mathring{A}^2) $\stackrel{*}{\underline{\cdot}}$	8.5	11.0	9.7	10.3

[#] If mean $I/\sigma(I)$ in outer shell is <2.0, please provide an explanation [as a footnote here] and provide resolution at which it falls below 2.0.

Table 2 Structure solution and refinement Values for the outer shell are given in parentheses.

huHf + Fe(II) 1 min 5 min 15 min 30 min

[†] Only the redundancy-independent merging R factor $R_{\text{r.i.m.}}$ or R_{meas} should be reported. If these values are not available, they may be estimated by multiplying the conventional R_{merge} value by the factor $[N/(N-1)]^{1/2}$, where N is the data multiplicity [in such cases, provide a footnote here].

[‡] State here if there are any anomalies in the Wilson plot, such as spikes arising from ice rings, etc.

PDB code	4Y08	4ZJK	4OYN	4YKH
Resolution range (Å)	27.76–1.34	31.07–1.56	31.09–1.43	28.07-1.52
Resolution range (71)	(1.38–1.34)	(1.60–1.56)	(1.47-1.43)	(1.56–1.52)
Completeness (%)	99.7 (100.0)	99.7 (98.3)	100.0 (100.0)	99.9 (100.0)
σ cutoff	2.0	2.0	2.0	2.0
No. of reflections, working set	56945 (4127)	36303 (2592)	47040 (3384)	39434 (2874)
No. of reflections, test set	3037 (230)	1918 (124)	2508 (190)	2086 (139)
Final R _{cryst}	0.163 (0.175)	0.168 (0.202)	0.167 (0.183)	0.165 (0.171)
Final R _{free}	0.173 (0.190)	0.192 (0.237)	0.179 (0.214)	0.187 (0.180)
Cruickshank DPI	0.043	0.068	0.053	0.062
No. of non-H atoms				
Protein	1409	1413	1413	1410
Ion	19	24	23	23
Ligand	4	-	19	11
Water	328	329	320	323
Total	1760	1766	1775	1676
R.m.s. deviations				
Bonds (Å)	0.006	0.007	0.005	0.006
Angles (°)	1.037	1.000	0.981	1.007
Average B factors (\mathring{A}^2)				
Protein	10.2	13.7	11.7	12.9
Ion	13.9	20.3	16.1	16.4
Ligand	9.2	0.0	22.5	9.5
Water	23.6	29.4	26.2	27.8
Estimate error on coordinates based on R value (Å)	0.043	0.068	0.053	0.062

Ramachandran plot					
Most favoured (%)	98.8	98.8	98.8	98.8	
Allowed (%)	1.2	1.2	1.2	1.2	

Figure 1 Ribbon diagram of the HuHf subunit represented as ribbon rainbow coloured from N-terminus (blue) to C-terminus (red). The five α -helices are sequentially numbered starting from the N-terminus. The oxidoreductase site (OS) and the 3-fold and 4-fold pore locations are shown by arrows pointing into the ferritin cage interior together with amino acid residues involved in iron binding.

Figure 2 a) Electron density in HuHf oxidoreductase site after 1 minute of iron free diffusion into the crystals. The 2Fo-Fc map is represented as light blue wire (1.5σ) , while the residual Fo-Fc difference map contoured at 3.0 σ is represented as green wire. The copper wires represent the anomalous difference map contoured at 4.0 σ . The protein backbone is represented as light blue cartoon and residues involved in iron coordination are highlighted as yellow sticks. The disorder present in some side chains is visualized as double conformations. Iron ions are represented as green spheres. b) Our interpretation of the electron density maps shown in 1A. Two "dioxygen-like" molecules are represented as sticks. The 2Fo-Fc map is contoured at 1.5 σ (light blue wire). The Fo-Fc Fourier difference map is featureless at 3.0 σ .

Figure 3 a) Electron density in HuHf oxidoreductase site after 5 minutes of exposure to Mohr's salt. The Fourier maps and anomalous difference map contours and colors are the same as in Figure 1. b) Schematic view of the OS of HuHf. Coordination bonds are shown as black continuous lines, H-bonds are represented by dotted lines. The color codes are the same used in Figure 1.

Figure 4 Views perpendicular (a) and along (b) the 3-fold axis pore of HuHf as appearing in the crystal structure obtained after 15 minutes of free diffusion of iron ions inside the crystal. The 2Fo-Fc and the anomalous difference maps are superimposed to the atomic model. The cutoffs and the color codes are the same used in previous Figures.

Figure 5 View of the 4-fold axis pore of HuHf as appearing in the crystal structure obtained after 5 minutes and onwards. The 2Fo-Fc and the anomalous difference maps are superimposed to the atomic model. The cutoffs and the color codes are the same used in previous Figures.

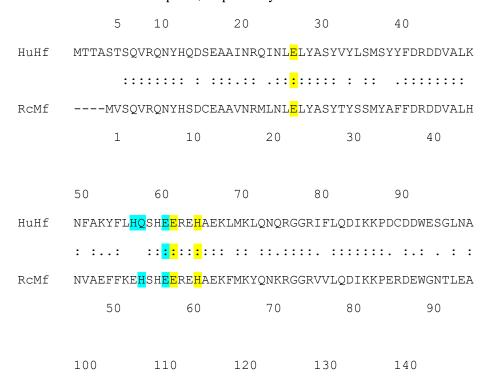
Figure 6 *a)* The catalytic reaction rate in HuHf and RcMf are differently modulated by the Fe²⁺/subunit ratio. Comparison of the reaction kinetic of (left) DFP intermediate (A_{650nm}) and (right) (DFO(H)) products (A_{350nm}) formation after the addition of 1, 2, 3, 4 Fe²⁺/subunit to HuHf (upper panels) and RcMf (lower panels). *b)* The panels show the dependency on the Fe²⁺/subunit ratio of the initial rates of formation of DFP (left), decay of DFP (middle) and formation of DFO(H) (right).

Figure 7 Biomineral core characterization. Representative TEM micrographs of HuHf and RcMf caged biomineral obtained from 2.5 μ M solutions of each protein mineralized with ferrous sulfate (80 Fe²⁺/subunit). The samples are not negatively stained, thus the observed density represents the iron core within ferritin and not the protein.

Figure 8 Least squares superimposition of the OS of HuHf (pale blue ribbon) and RcMf (pale yellow ribbon). The different locations and ligands of Fe3, Fe4 and Fe5 iron binding sites are evident. The amino acids are represented as sticks colored following the color of the parent protein backbone.

Supporting information

Figure S1 Amino acid sequence alignment prepared with EMBOSS (Rice *et al.*, 2000). The different numbering of the two sequences is maintained. Yellow bars highlight the residues acting as iron ligands of Fe1 and Fe2, the cyan bars the amino acids in additional binding sites in the oxydoreductase cavity, the green and the magenta bars indicate the residues involved in the interactions with Fe-aquaions or Fe binding in the 3-fold and four-fold axis pores, respectively.



HuHf	MECALHL <mark>E</mark> K	INVNQSLLELI	HKLATDKNDPI	HLC <mark>D</mark> FI <mark>E</mark> THYLN	IEQVKAIKELG
	:. :: : <mark>:</mark> :	:::.:::	:::::::	::: <mark>:</mark> :. <mark>:</mark> . ::	:::: :: .:
RcMf	MQAALQL <mark>E</mark> K	TVNQALLDL	HKLATDKVDPI	HLC <mark>D</mark> FL <mark>E</mark> SEYLE	EQVK <mark>d</mark> ikrig
	100	110	120	130	140
	150	160	170	180	
HuHf	DHVTNLRKMGAPESGLAEYLFDK <mark>H</mark> TLGDSDNES				
	: .:::	: ::.:: ::	::::: <mark>:</mark>	:	
RcMf	DFITNLKRI	GLPENGMGE	YLFDK <mark>h</mark> SVKE:	SS	
	150	160	170		